Atmospheric Research 277 (2022) 106287

Contents lists available at ScienceDirect

Atmospheric Research

journal homepage: www.elsevier.com/locate/atmosres

Nexus of ambient flow and squall line via turbulence in the March 2018 meso-scale convective system over Southeast China

Ziyu Guo [a], X. San Liang [b,c,*]

[a] School of Atmospheric Sciences, Nanjing University of Information Science and Technology, Nanjing 210044, China
[b] Department of Atmospheric and Oceanic Sciences, Fudan University, Shanghai 200348, China
[c] Division of Frontier Research, Southern Marine Science and Engineering Guangdong Laboratory (Zhuhai), Zhuhai 519000, China

ARTICLE INFO

Keywords:
Squall line
Multiscale energetics
Multiscale window transform
Canonical transfer
Turbulence

ABSTRACT

On March 4, 2018, an extremely strong squall line occurs suddenly over Southeast China, incurring devastatingly strong surface winds. In this study, we first present a high-resolution model simulation, then apply the recently developed theory of canonical transfer, which bears a form reminiscent of the Poisson bracket in Hamiltonian mechanics, to investigate the underlying dynamical processes. Using a recently developed functional analysis apparatus, multiscale window transform, the fields are reconstructed onto three scale windows, namely, ambient flow window, squall line-scale window, and turbulence window, which for convenience are denoted as windows 0, 1, 2, respectively. It is found that, among all the canonical transfers of kinetic energy (KE), only that between windows 0 and 2, and that between windows 1 and 2, are significant, and the two correspond remarkably well in space, except for opposite signs. Specifically, at the leading edge, KE is first transferred from the ambient flow over the spectrum all the way to the turbulence scale processes, and then goes to window 1 to form the squall line. At the trailing edge, this process is reversed. While the downscale cascading at the leading edge and upscale transfer at the trailing edge are expected in the classical shock hypothesis of squall lines, the existence of the secondary upscale and downscale transfers, respectively, at the leading and trailing edge, are not seen before. Most importantly, these secondary canonical transfers make the turbulence-scale window function like a hub, bridging the ambient flow and the squall line. To our knowledge, such an energetic scenario, i.e., the nexus of two adjacent scales in a spectrum via a "remote mediator" is not seen before in the literature. This study testifies to the importance of turbulent flows in the maintenance of squall lines, and may yield a clue to a better simulation.

1. Introduction

Squall lines, also called as quasi-linear convective systems (Weisman and Davis, 1998), or bow echoes in Doppler radar (Nolen, 1959; Przybylinski, 1995), may cause widespread straight-line damaging winds and even tornados (Fujita, 1978; Atkins et al., 2005; Wakimoto et al., 2006a, 2006b). On 4 March 2018, a squall line with strong surface wind occurs in Southeastern China, incurring heavy casualties and economic loss. It moves northeastward from Guangxi to Zhejiang, covering most part of the Yangtze Valley Plain (Fig. 1). The convection is originally triggered in Guangxi (Fig. 1a) at 04:00 UTC on 4 March, gradually organized (Fig. 1b) and developed into a meso-scale convective system (MCS), with a convective line formed after 06:00 UTC (Fig. 1c–e). The MCS moves southeastward and becomes weaker after leaving Zhejiang at 12:00 UTC (Fig. 1f).

Generally, a squall line contains a "leading-line/trailing-stratiform" structure, with rear inflow and front-to-rear (storm relative) flow with updrafts and downdrafts driven by a cold pool (Ogura and Liou, 1980; Weisman, 1992; LeMone et al., 1984). The cold-pool circulation is originated from the mid-level stratiform region, and this "rotor" circulation, which is driven by the buoyancy in the head region of the density current/cold pool (Xu and Moncrieff, 1994), maintains a close relationship between the convection and the mesoscale environment (Lafore and Moncrieff, 1989). In idealized model studies, it is usually simplified as a steady gravity current (Benjamin, 1968). With respect to the bow echo line, the part of the stratiform ahead of it is called as "forward anvil", and that lying behind is the "trailing stratiform". The squall line stratiform structure can be classified into 3 types (c.f., Parker and

* Corresponding author at: Department of Atmospheric and Oceanic Sciences, Fudan University, Shanghai 200348, China.
E-mail address: xsliang@fudan.edu.cn (X.S. Liang).

https://doi.org/10.1016/j.atmosres.2022.106287
Received 8 February 2022; Received in revised form 3 June 2022; Accepted 3 June 2022
Available online 7 June 2022

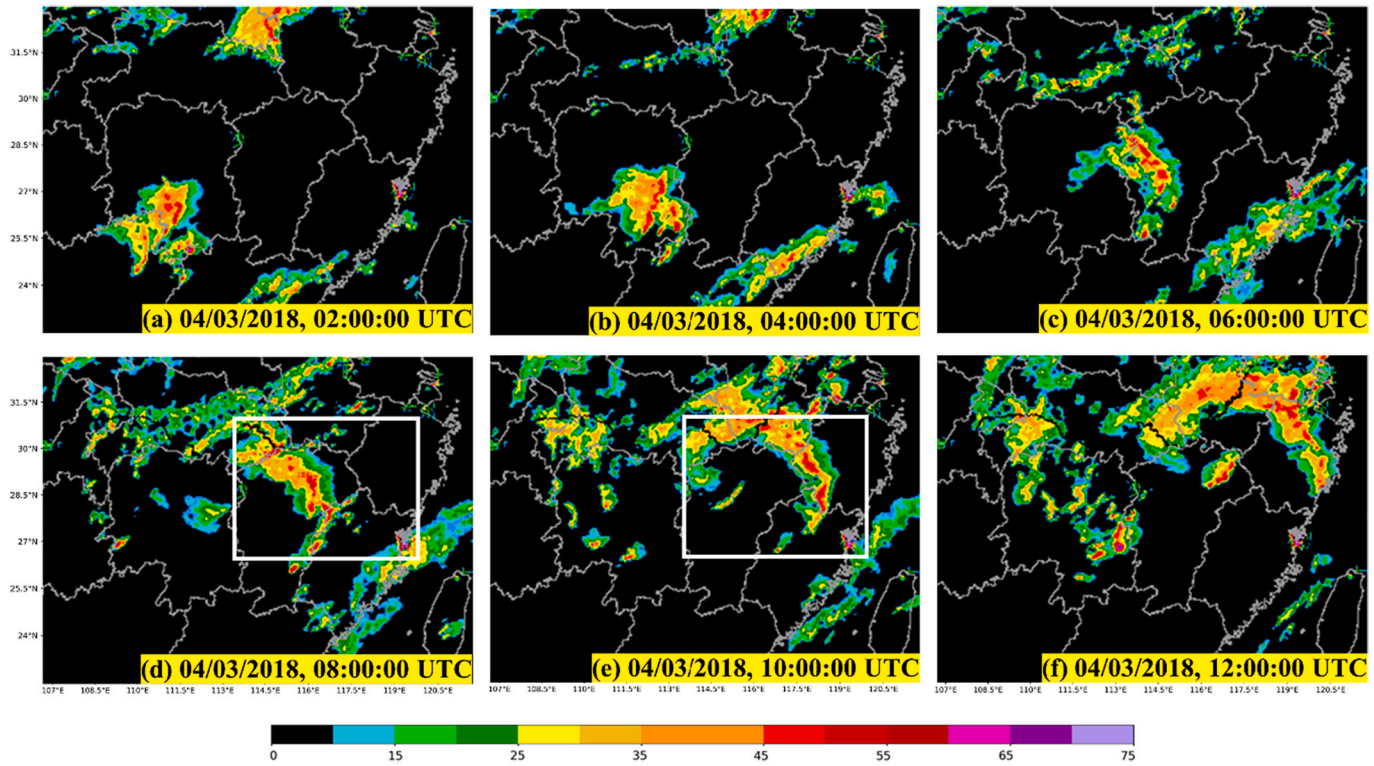

Fig. 1. Radar mosaic showing the radar reflectivity (in dBZ) at (a) 02:00 UTC, (b) 04:00 UTC, (c) 06:00 UTC, (d) 08:00 UTC, (e) 10:00 UTC, and (f) 12:00 UTC on 4 March 2018. The white box is the innermost domain of our nested model. Also shown are the boundaries between the provinces. The composite radar reflectivity data are selected from the two stations Sanming and Jianyang.

Johnson, 2000), according to the location of convective lines relative to stratiform precipitation, as trailing (TS type), leading line (LS type), and parallel (PS type) stratiform precipitations. Depending on the stage in a squall line life cycle, one type may be changed to another. By statistics the bow echo structure is mostly symmetric in structure. The symmetry reveals that squall lines are well organized. But, when a squall line is weakened, the structure may also become asymmetric (Houze et al., 1990), which, as we will see soon, also exists in the case of this study (Sheng, 2019). At the front (or leading edge) intense winds and thermal gradients exist, where cold air subsidies from ~3 km high to surface, making a cold pool of about 1 km thick (Charba, 1974). As for the ambient environment, usually the vertical wind shear is large (Li and Wu, 2020)—It has been related to the longevity of squall lines (Rotunno et al., 1988).

Squall line simulation is faced with many problems, one of which is the existence of energy-containing vortices in sub-grids. In mesoscale modeling, the scales of some energy-containing turbulent structures are much smaller than the scale of the spatial filter. Even in highly resolved squall line simulations, there exists a large portion of in-cloud-scale turbulences energy; for instance, Bryan et al. (2003) show that the ratio of the sub-grid turbulence kinetic energy (TKE) to the total TKE even exceeds to 10%. This subgrid regime, called “terra incognita” or “gray zone”, poses a great challenge to mesoscale simulation (Wyngaard, 2004). Recent studies show that this kind of unsuitable selection of horizontal resolution may lead to a suppression of the entrainment and detrainment processes (Lebo and Morrison, 2015), and may bring error to the downdraft strength (Varble et al., 2020), and hence impact the squall line storm's evolution. Although many studies support the hypothesis that increasing horizontal grid density can lead to more precise squall line structure (Lilly, 1990; Potvin and Flora, 2015; Zhang et al., 2021), and some studies find that squall lines can be well-simulated with a 4-km resolution grid (Weisman et al., 1997), so far it is still unclear what resolution is most suitable. Besides, as commented by Bryan et al. (2003), “future studies should also explore the resolution sensitivity of different types of convection, such as an unorganized complex of convective cells or perhaps a line of supercells.”

The most prominent feature of squall lines is the discontinuity near the gust front, which forms a formidable challenge in modeling. Along the echo bow line, the sharp pressure gradient shows as hydraulic jumps (Frame and Markowski, 2006), or shockwaves in compressible gas (Tepper, 1950). Pressure jumps may occur when gravity wave sources (like cold fronts) accelerate, with waves propagating faster than the background wind speed. The relation between the velocity of the flow and that of the waves can be expressed in terms of Fraude number (surface wave in density current model) and Mach number (sound wave in compressible gas). A “head wave” (the leading edge of gravity wave) forms when the Froude number is high enough, followed by a wave breaking region in the rearward side, with energy dissipated into turbulence (Benjamin, 1968; Charba, 1974). The head wave in a two-layer model (also referred to as inversion layers, meaning a colder layer with higher density under a warmer layer) can well describe a squall line's discontinuity (Tepper, 1950), but the model setting is too simple to represent the realistic environment about the squall line. Lindzen and Tung (1976) extend this two-layer model to a wave-duct model, by considering the vertical propagation and reflection of gravity waves in a vertical shear environment (stratified flow). Majda and Xing (2010) develop a multi-scale squall line model governed by Taylor-Goldstein equations, which are usually used to describe the stratified flow in a quasi-two-dimensional (2D) shear environment. They find that, as the environment shear becomes stronger, upscale turbulent eddy fluxes will develop. Bryan et al. (2003) find the transition process from a laminar flow to turbulence is mainly dominated by Kelvin–Helmholtz instabilities near the cold pool, and the resulting turbulence hence influences the vertical motions around the squall line through upscale cascading. Recent numerical simulations also confirm the existence of backscatter (upscale cascading) in squall lines (e.g., Lai and Waite,

2020).

The backscatter as described above raises a serious issue in squall lines simulation. Traditional models for large-eddy simulation (LES) are absolutely dissipative (Smagorinsky, 1963; Kraichnan, 1976; Deardorff, 1980); they remove energy from the large scales at each point in the physical space, without transfer energy back to the large scales (backscatter) at a given location (Piomelli et al., 1991). So far backscatter process can only be represented through direct numerical simulation (DNS) which is infeasible for the modeling of large-scale fluid flows such as atmospheric circulation, many studies hence focus on implementing turbulence closure in the LES scheme. This inclues the nonlinear backscatter and anisotropy model (Kosović, 1997), dynamic reconstruction model (Chow et al., 2005), Lagrangian-averaged scale-dependent model (Bou-Zeid et al., 2005), and stochastic backscatter model (Leith, 1990; Schumann, 1995), to name several. However, comparing to the traditional Smagorinsky model (Smagorinsky, 1963), these models are computationally much more expensive (Kirkil et al., 2012).

All these researches point to the importance of turbulence-like small scale processes; however, the role of these processes is still mostly unclear. In this study, based on a relatively successful simulation of the March 2018 squall line event in Southeast China, we hope to gain some insight into the dark side of the underlying dynamics, by employing a recently developed multiscale analysis tool, namely, multiscale window transform (MWT), and an MWT-based theory on energy transfer. In the following, we first give a brief introduction of MWT, and the theory of canonical transfer (Section 2). After that a real-time simulation is made for the March 2018 squall line (Section 3). The MWT is set up in Section 4. Section 5 shows the reconstructed fields on the squall line scale window or meso-beta-scale window. In Section 6, the canonical transfers are analyzed, and the major results of this study are presented therein. This study is summarized in Section 7.

2. Multiscale window transform (MWT), canonical transfer, and localized multiscale energetics

As is well known, the Reynolds formalism of multiscale energetics based on time averaging are invariant in time, and those formulated with zonal mean do not have information in longitude, etc. Such formalisms cannot be used to study the energy burst processes such as squall lines which are highly localized in space and time. To overcome the difficulty, during the past decades, filtering has been widely used to replace the time averaging in the above formalism. Now a fundamental question arises: what is the corresponding energy for a filtered field? A common practice widely exercised during the past decades is simply to square the filtered field and take it as the energy (up to some proportionality). This is, unfortunately, conceptually incorrect. To illustrate, suppose we are given a time series u(t), which has only two harmonic components with frequencies ω_0 and ω_1,

$$u(t) = \underbrace{a_0 cos\omega_0 t + b_0 sin\omega_0 t}_{u_L(t)} + \underbrace{a_1 cos\omega_1 t + b_1 sin\omega_1 t}_{u_H(t)}. \quad (1)$$

For this simple example, we know that the energies for the two components are $a_0^2 + b_0^2$ and $a_1^2 + b_1^2$, respectively. That is to say, the energies are the squares of the respective transform coefficients. They are absolutely not equal to the square of the respective reconstructed (filtered) fields, i.e., $u_L[(t)]^2$and $[u_H(t)]^2$. In other words, multiscale energy is a concept with the transform coefficients defined in phase space (independent of t here), while $u_L[(t)]^2$and $[u_H(t)]^2$ are quantities in physical space (as functions of t). These two are related through the well-known Parseval's identity in functional analysis. Particularly, when $u_L[(t)]^2$ is a constant (i.e., time mean), we can obtain $a_1^2 + b_1^2 = \overline{u_H[(t)]^2}$ (the overbar denotes the time-averaging operator). This explains why the time-averaging operator in the classical Reynolds decomposition-based energetics formalism is necessary; otherwise the resulting energetics do not make sense in physics.

Table 1
The energetic terms in Eqs. (2)–(3). The notations are conventional in primitive atmospheric equations (cf. Liang, 2016).

Symbol	Expression	Physical meaning
K^{ϖ}	$\frac{1}{2}\widehat{\mathbf{v}}_h^{\sim\varpi} \bullet \widehat{\mathbf{v}}_h^{\sim\varpi}$	KE on scale window ϖ
$\boldsymbol{Q}_K^{\varpi}$	$\frac{1}{2}\widehat{(\mathbf{v}\mathbf{v}_h)}^{\sim\varpi} \bullet \widehat{\mathbf{v}}_h^{\sim\varpi}$	Flux of KE on window ϖ
Γ_K^{ϖ}	$\frac{1}{2}\left[\widehat{(\mathbf{v}\mathbf{v}_h)}^{\sim\varpi} : \nabla\widehat{\mathbf{v}}_h^{\sim\varpi} - \nabla \bullet \widehat{(\mathbf{v}\mathbf{v}_h)}^{\sim\varpi} \bullet \widehat{\mathbf{v}}_h^{\sim\varpi}\right]$	Canonical transfer of KE to window ϖ
$\boldsymbol{Q}_P^{\varpi}$	$\widehat{\mathbf{v}}^{\sim\varpi}\widehat{\Phi}^{\sim\varpi}$	Pressure flux
b^{ϖ}	$\widehat{\omega}^{\sim\varpi}\widehat{\alpha}^{\sim\varpi}$	Buoyancy conversion
A^{ϖ}	$\frac{1}{2}c\left(\widehat{\Gamma}^{\sim\varpi}\right)^2, c = \frac{g}{\overline{T}(g/C_p - L)}$	APE on scale window ϖ
$\boldsymbol{Q}_A^{\varpi}$	$\frac{1}{2}c\widehat{\Gamma}^{\sim\varpi}\widehat{(\mathbf{v}\Gamma)}^{\sim\varpi}$	Flux of APE on window ϖ
Γ_A^{ϖ}	$\frac{c}{2}\left[\widehat{(\mathbf{v}\Gamma)}^{\sim\varpi} \bullet \nabla\widehat{\Gamma}^{\sim\varpi} - \widehat{\Gamma}^{\sim\varpi}\nabla \bullet \widehat{(\mathbf{v}\Gamma)}^{\sim\varpi}\right]$	Canonical transfer of APE to window ϖ
S_A^{ϖ}	$\frac{1}{2}\widehat{\Gamma}^{\sim\varpi}\widehat{(\omega\Gamma)}^{\sim\varpi}\frac{\partial c}{\partial p} + \frac{1}{\overline{T}}\widehat{\omega\alpha}^{\sim\varpi}$	Apparent source/sink (usually negligible)

If total energetics (in W) are to be computed, the resulting integrals with respect to (x, y, p) should be divided by g. Besides, all terms are to be multiplied by 2^{j_2}, which is omitted for notational simplicity.

It is, therefore, a rather complex and profound problem to have the local energy of a time-dependent filtered field faithfully represented. In fact, this has not been feasible until filter banks and wavelets are connected, and has just been systematically addressed by Liang and Anderson (2007) in the development of multiscale window transform (MWT).

MWT is an apparatus decomposing a function space into a direct sum of orthogonal subspaces, each with an exclusive range of scales (represented by wavelet scale levels). Such a subspace is termed a scale window, or simply a window. MWT is originally developed for representing the energies on the resulting multiple scale windows, in order to make multiscale energetics analysis possible. Liang and Anderson (2007) find that, for some specially constructed orthogonal filters, there exists a transfer-reconstruction pair, just as the Fourier transform and inverse Fourier transform. (Note here orthogonality is crucial; otherwise the Parseval identity does not hold, and hence energy cannot even be defined.) This pair is the very MWT and its peer, namely, multiscale window reconstruction (MWR). Loosely speaking, the MWR of a series $S(t)$ results in a filtered series, while the corresponding MWT coefficients can give the energy of that filtered series. This is in contrast to the traditional filters; they yield only filtered fields (reconstructions), without transform coefficients.

In MWT, a scale window is demarcated on the wavelet spectrum by two scale levels, or window bounds. For a time series with a duration τ, a scale level j corresponds to a period $2^{-j}\tau$. Obviously, the number of time steps need to be a power of 2. In this study, we will need three scale windows, which are bounded above by three wavelet scale levels: j_0, j_1 and j_2. Alternatively, $2^{-j_0}\tau$, $2^{-j_1}\tau$ and $2^{-j_2}\tau$ are the time scale bounds. For convenience, we will henceforth refer to them as ambient/background flow window, meso-beta scale or squall line window, and turbulence scale window, and will denote them by $\varpi = 0, 1, 2$, respectively. The decomposition will be justified later in the wavelet power spectral analysis in Section 4.

Given a time series S{(t)}{S(t)}, application of MWT yields a transform coefficient $\widehat{S}_n^{\sim\varpi}$ $[\widehat{(\bullet)}_n^{\sim\varpi}$ denotes MWT on window ϖ at time step n], and a reconstruction on window ϖ, written $S^{\sim\varpi}(t)$. It has been proved that the energy on window ϖ is proportional to $\left(\widehat{S}_n^{\sim\varpi}\right)^2$. Note it is by no means as trivial as $[S^{\sim\varpi}(t)]^2$, i.e., the square of the filtered field! This is how MWT is different from the existing filters. With these, Liang (2016) shows that the multiscale kinetic energy (KE) and available potential energy (APE) equations are, for windows ϖ (=0, 1, 2),

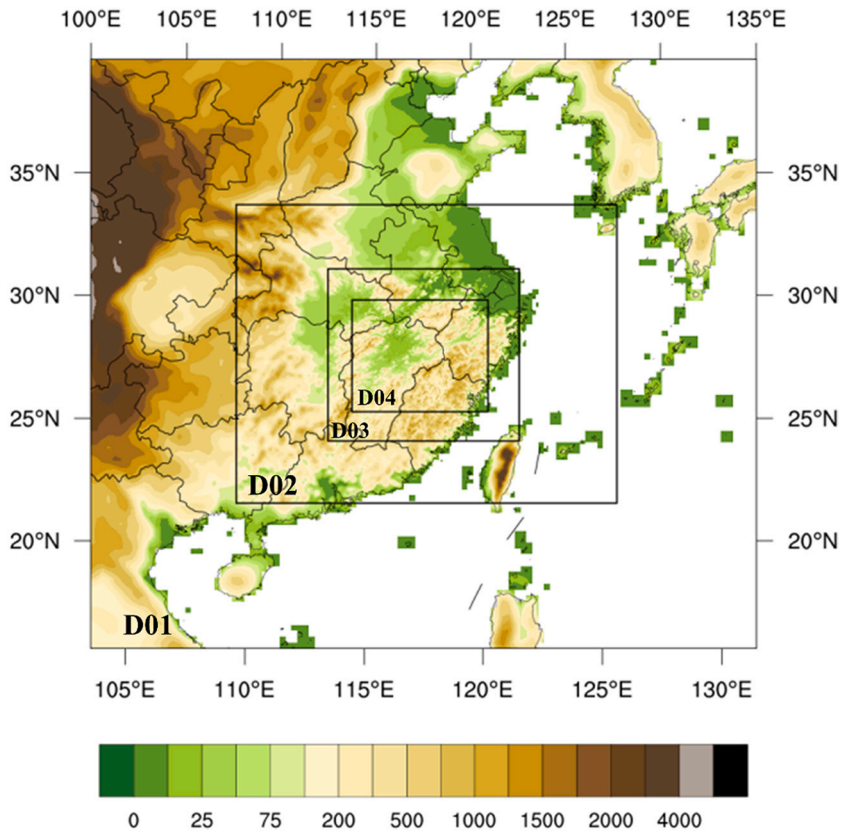

Fig. 2. The grid configuration used for the WRF-ARW simulation. The four nested domains (from D01 to D04) are marked by black rectangles. The terrain shaded by colors.

$$\frac{\partial K^{\varpi}}{\partial t}+\nabla\bullet\mathbf{Q}_K^{\varpi}=\Gamma_K^{\varpi}-\nabla\bullet\mathbf{Q}_P^{\varpi}-b^{\varpi}+\mathrm{F}_{K,p}^{\varpi}+\mathrm{F}_{K,h}^{\varpi}, \tag{2}$$

$$\frac{\partial A^{\varpi}}{\partial t}+\nabla\bullet\mathbf{Q}_A^{\varpi}=\Gamma_A^{\varpi}+b^{\varpi}+\mathrm{S}_A^{\varpi}+\mathrm{F}_A^{\varpi}. \tag{3}$$

(For simplicity here the time step n is suppressed.) The explanations and expressions for these terms are listed in Table 1. Among these terms, the Γ terms represent transfers between different scale windows; they are very different from those in classical formalisms. Particularly, there is an interesting property, i.e.,

$$\sum_{\varpi}\left(\sum_{n}\Gamma_n^{\varpi}\right)=0,$$

as first shown in Liang and Robinson (2005) and later on rigorously proved (see Liang, 2016). Physically this means that the energy transfer is a mere redistribution of energy among the scale windows, without generating or destroying energy as a whole. This property, though simply stated, does not hold in previous time decomposition-based or Lorenz-type energetics formalisms (see below). To distinguish, such as transfer is termed "*canonical transfer*". A canonical transfer has a Lie bracket form that satisfies the Jacobian identity, reminiscent of the Poisson bracket in Hamiltonian mechanics; see Liang (2016) for details.

To see how a canonical transfer differs from the energy transfer in classical energetics formalisms, consider a passive tracer T (may be any scalar field; need not be temperature) in an incompressible flow, and neglect all other processes but for advection:

$$\frac{\partial T}{\partial t}+\nabla\bullet(\mathbf{v}T)=0. \tag{4}$$

By applying a traditional Reynolds decomposition, it yields the mean and perturbation equations

$$\frac{\partial\overline{T}}{\partial t}+\nabla\bullet(\overline{\mathbf{v}}\,\overline{T}+\overline{\mathbf{v}'T'})=0, \tag{5}$$

$$\frac{\partial T'}{\partial t}+\nabla\bullet(\mathbf{v}'\overline{T}+\overline{\mathbf{v}}T'+\mathbf{v}'T'-\overline{\mathbf{v}'T'})=0. \tag{6}$$

Multiplying (5) by $\overline{T}$, and (6) by T′, followed by an averaging, one arrives at the evolutions of the mean energy and eddy energy (variance) (e.g. Pope, 2004)

$$\frac{\partial\overline{T}^2/2}{\partial t}+\nabla\bullet(\overline{\mathbf{v}}\,\overline{T}^2/2)=-\overline{T}\nabla\bullet(\overline{\mathbf{v}'T'}), \tag{7}$$

$$\frac{\partial\overline{T'^2/2}}{\partial t}+\nabla\bullet\left(\frac{\overline{\mathbf{v}T'^2}}{2}\right)=-\overline{\mathbf{v}'T'}\bullet\nabla\overline{T}. \tag{8}$$

The terms in divergence form are generally understood as the transports of the mean and eddy energies, and those on the right hand side as the respective energy transfers during the mean-eddy interaction. Particularly, when T is a velocity component, the right side of (8), $\mathrm{R}=-\overline{\mathbf{v}'T'}\bullet\nabla\overline{T}$, has been interpreted as the rate of energy extracted by Reynolds stress against the mean profile; in the context of turbulence research, it is also referred to as the "rate of the turbulence production" (Pope, 2004). It has been extensively utilized in geophysical fluid dynamics for the explanation of the phenomena such as cyclogenesis, eddy shedding, etc. However, Holopainen (1978) and Plumb (1983) have argued that the transport-transfer separation is ambiguous, and hence the resulting transfer is physically not robust. Moreover, Eqs. (7) and (8) do not, in general, sum to zero on the right hand side. This is not what one would expect of an energy transfer, which by physical intuition should be a redistribution of energy among scale/scale windows, and

should not generate nor destroy energy as a whole.

With the MS-EVA formalism, the above are not issues any more. In this special case the energy Eqs. (7) and (8) are reduced to (see Liang, 2016),

$$\frac{\partial \overline{T}^2/2}{\partial t} + \nabla \bullet \left(\frac{1}{2}\overline{\mathbf{v}}\overline{T}^2 + \frac{1}{2}\overline{T}\overline{\mathbf{v}'T'} \right) = -\Gamma, \tag{9}$$

$$\frac{\partial \overline{T'^2/2}}{\partial t} + \nabla \bullet \left(\frac{1}{2}\overline{\mathbf{v}T'^2} + \frac{1}{2}\overline{T}\overline{\mathbf{v}'T'} \right) = \Gamma, \tag{10}$$

where $\Gamma = \frac{1}{2}\{\overline{T}\nabla \bullet (\overline{\mathbf{v}'T'}) - (\overline{\mathbf{v}'T'})\nabla\overline{T}\}$. Now one can see that the right hand side is balanced, in contrast to Eqs. (7) and (8). We hence call this Γ a "canonical transfer". As shown by Liang (2016), it has a Lie bracket form. Previously, Liang and Robinson (2007) illustrate, for a benchmark hydrodynamic instability model whose instability structure is analytically known, the traditional Reynolds stress extraction $R = -\overline{\mathbf{v}'T'} \bullet \nabla\overline{T}$ does not give the correct source of instability, while Γ does.

Note a canonical transfer to a window ϖ may involve contributions from different windows; we need to differentiate them to trace the dynamical source. This is done by a procedure called "interaction analysis," explained in detail in Liang and Robinson (2005). Here we only indicate it symbolically, say, as $\Gamma_K^{j\to i}$ for canonical KE transfer from window j to window i. So $\Gamma_K^{1\to 2}$ means canonical KE transfer from the meso-β-scale window ($\varpi = 1$) to the turbulence scale window ($\varpi = 2$), so and so forth.

3. Simulation of the March 2018 Southeast China squall line

Squall line simulation is faced with many problems, one of which is the existence of energy-containing vortices in sub-grids. In mesoscale modeling, the scales of some energy-containing turbulent structures are much smaller than the scale of the spatial filter. Even in highly resolved squall line simulations, there exists a large portion of in-cloud-scale turbulences energy, which violates the energy-containing vortices assumption. Although many studies support the hypothesis that increasing horizontal grid density can lead to more precise squall line structure (Lilly, 1990; Potvin and Flora, 2015; Zhang et al., 2021), and some studies find that squall lines can be well-simulated with a 4-km resolution grid (Weisman et al., 1997), so far it is still unclear what resolution is most suitable. So far, no real time squall line simulation can be said successful; to get a satisfactory simulation is still a huge challenge.

In this study, however, we have made a relatively successful simulation of the March 2018 squall line over Southeast China, though the relative success could be accidental. Although the lasting duration is not long, this dataset is satisfactory enough to allow us to perform an in-depth analysis which will, hopefully, reveal to us some aspects of the dynamics underlying realistic squall lines.

The simulation is conducted using the Advanced Research Weather Research and Forecasting Model (ARW-WRF ver. 4.0, Skamarock et al., 2008). The model has a four-layer nesting. The domains are named as, from the largest to the smallest, D01, D02, D03, and D04; see Fig. 2. The first three are two-way nested, while that between D03 and D04 is one-way. D01 covers much of Southeastern China at a 27-km grid spacing, with 115 × 102 horizontal grid points (Fig. 2), including the regions during the period of concern the squall line sweeps. The other 3 sub-domains have spatial resolutions of, respectively, 9 km, 3 km, and 1 km. The innermost domain, namely D04, at a 1-km grid spacing, has 514 × 628 horizontal grid points. It covers the core region where the squall line is formed (see the white box in Fig. 1d–e). All of these domains have 31 vertical levels extending from the surface to 50 hPa. Physical process parameterization schemes are identical for the four domains, including shortwave radiation (Dudhia, 1989), Rapid Radiative Transfer Model longwave radiation (Mlawer et al., 1997), Noah land surface model with four soil layers (Niu et al., 2011), Kain–Fritsch convective scheme (Kain, 2004), the Morrison 2-moment scheme (Morrison et al., 2009), and the Mellor-Yamada-Janjic (Eta) TKE scheme (Janjić, 1994). The convective scheme is adopted only in D01-D02, where horizontal resolution is higher than 5 km. Initial conditions (ICs) and boundary conditions (BCs) are updated every 6 h using the 0.25° × 0.25° NCEP FNL (Final) operational global analysis and forecast data. These, and other parameters, are summarized in Table 2.

Table 2
Summary of the settings for the WRF model simulation.

Δx, Δy for	27–9–3 km, two-way nested
The 4 nested domains	1 km, one-way nested
Vertical levels	31
Δz	~27.5–233.1 m
Model top	~19.2 km
Microphysical parameterization	Morrison 2-moment scheme (Morrison et al., 2009)
Turbulence parameterization	Mellor-Yamada-Janjic (Eta) TKE scheme (Janjić, 1994)
Radiation parameterization	RRTM–Dudhia scheme(Dudhia, 1989; Mlawer et al., 1997)
Land surface parameterization	Noah-Eta scheme (Niu et al., 2011)
Convective parameterization	Kain–Fritsch scheme (d01, d02 grid only) (Kain, 2004)
Initialization	FNL analysis, 08:00 UTC 3 March
Lateral boundary conditions	FNL analysis, every 6 h

The above simulation, though much limited, proves to be relatively successful from 18:00 UTC, March 3 to 12:00 UTC, March 4, 2018. In Fig. 3, the first row shows the observed radar reflectivity, while the middle row shows the corresponding simulation. Notice that the composite radar reflectivity data in Fig. 3a–c are selected from the two stations Sanming and Jianyang, since in this study, we only focus on the evolution of the squall line in its mature stage, which is located east of Jiangxi Province and west of Fujian Province. In Fig. 3a–c, the bow echo is represented in red, while in Fig. 3d–f, it is represented by the temperature discontinuity (the boundary line contrasting red to blue). Obviously, the relative success is easily seen. Particularly, the bow structure is similar (Fig. 3c & f), with a surface cold pool (relatively lower equivalent potential temperature shown in blue in Fig. 3d–f) and a rear inflow from mid-level (see Fig. 5a–c). This causes a strong horizontal wind shear near surface (black wind bar in Fig. 3d–f), and a rainfall near and behind the convective line (blue line in Fig. 3g–i).

For squall line which always appears as a fast-moving bow echo, a suitable cross-section to well capture its characteristics and dynamical processes needs to, rather than keep fixed, move with it. In this study, following the squall line, we choose the point where radar reflectivity reaches 45dBZ near the leading edge as the center (corresponding to the so-called "convective line" within squall line) at each latitude, from which 50 km are extended both eastward and westward to constitute a cross-section with a width of 100 km. For each selected section, the eastern and the western parts of it represent respectively the "front side" and the "rear side" of the eastward moving squall line. The green contours in Fig. 3d–f show that the cross-sections thus selected cover nearly the whole squall line in both zonal and meridional directions as it moves. To represent the general characteristics of and dynamical processes occurring within the moving squall line, an ensemble of theses cross-sections are used when plotting.

Of course, there also exists some discrepancy between the observation and simulation. Notably is that the simulated squall line (the red-blue boundary) occurs about 1.5 h later, and a little bit northward (cf. Fig. 3a–f).

4. MS-EVA setup

We set up the MS-EVA scale window bounds through wavelet spectral analysis. Displayed in Fig. 4 are the time series of a typical near

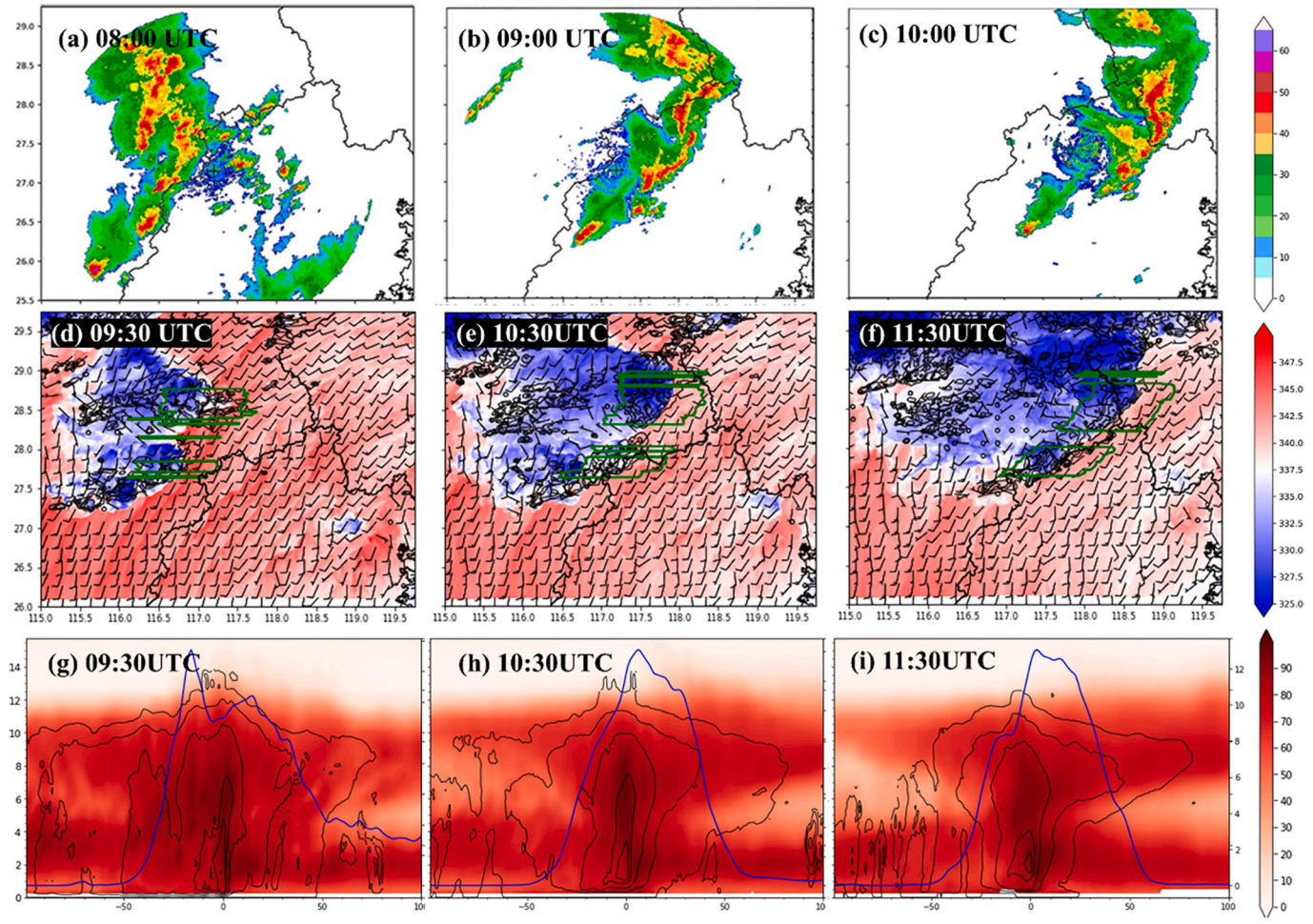

Fig. 3. Radar reflectivity at (a-c) 08:00, 09:00, and 10:00 UTC on 4 March as observed at Sanming and Jianyang Stations. (d-f) The simulated radar reflectivity (in 10dBZ, black lines) and equivalent potential temperature (K, shaded) at the bottom of the model. The contrast line marks the location of the simulated squall line. The green contours mark the cross-sections used in this study as produced by the method introduced in the text. (g-i) The vertical storm structure of the ensemble relative humidity (%, shaded) over those cross-sections at times corresponding to that in (d-f). The precipitation (per hour) is shown in blue line (mm). (For interpretation of the references to color in this figure legend, the reader is referred to the web version of this article.)

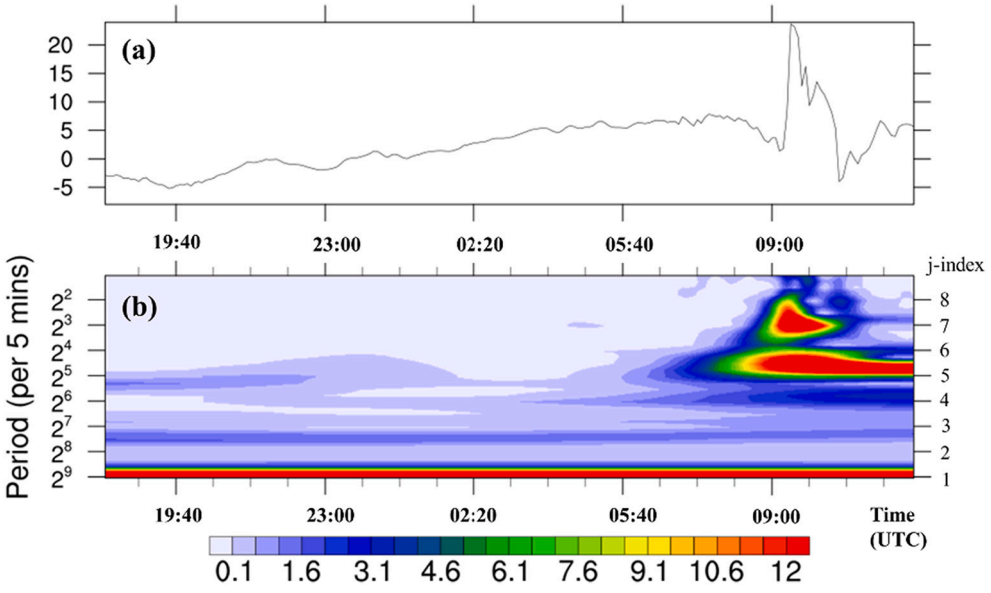

Fig. 4. (a) Time series of the 975 hPa (~280 m above surface) *u*-component wind (unit: m/s) at point (28.7° N, 117.0° E). (b) The wavelet power spectrum (m^2/s^2).

Table 3
The parameters used for our energetic analysis.

Index	Name	Scale level (j-index)	Period range
2	turbulence scale /meso-gamma-scale	$j > 6$	<1.3 h (hourly);
1	squall line scale / meso-beta-scale	$2 \le j \le 6$	1.3–21.3 h (hourly to daily);
0	ambient/background flow scale	$j < 2$	larger than 21.3 h (daily).

The scale window naming follows the convention of Orlanski (1975), according to their respective timescales.

surface wind and its wavelet spectrum. Clearly there are 3 peaks near the convection taking place. One is on the scale levels j = 6–7, corresponding to a period of 0.65–1.3 h, i.e., the hourly signal. The second peak is within j = 5–6 (1.3–2.6 h). Most of the energy is on the largest scale here, i.e., at scale levels j = 0–1, which are taken as the background flow. For this reason, we set the scale window bounds as: $j_0 = 2$, $j_1 = 6$ (see in Table 3). Since $2^6 = 64$, theoretically a time series of this length has complete information for the highest frequency process, i.e., the first peak in the spectrum. In this study, the time span of successful simulation results in a series of 216 time instants, which is long enough.

The above three-peak (or two-peak in the meoscale regime) spectrum has long been observed. Generally, squall line storm length is <250 km in China by statistics (Meng et al., 2013), which is, by classification, a meso-beta-scale process (Orlanski, 1975). Indeed it is reported that the meso-beta-scale process can describe the inner circulation of the squall line (Ducrocq and Bougeault, 1995). Also, studies find that turbulent scale processes also exist, such as the in-cloud turbulence, which impacts the microphysical process (Lynn et al., 2005a, 2005b; Lane et al., 2012), and the cloud-top turbulence wake in the lee of squall line (Pantley and Lester, 1990). Turbulence may deform along the dominant wind direction, especially near the gust front (Zhu et al., 2021). In squall line simulations, turbulent scale processes are important; they are represented in the planetary boundary layer (PBL) scheme, 2-D horizontal turbulence mixing schemes, and microphysics scheme (Weisman et al., 2008; Morrison et al., 2009; Lai and Waite, 2020), which have been mentioned in the preceding section. The two-peak structure of the mesoscale power spectra in deep convection simulation has also been found in Moeng et al. (2009, 2010). One peak is shown in the turbulence scale regime (as energy-containing turbulence), another in the cloud-system scale (as mesoscale cloud clusters). This from another aspect testifies to the validity of our simulation. We henceforth will refer to windows 0, 1, 2 as background flow window, squall line window, and turbulence window, respectively.

Other parameters in the MS-EVA setting are the horizontal resolution (1 km) and temporal resolution (300 s), which are in accordance with the WRF outputs. These outputs are taken as the MS-EVA input fields, including geopotential, temperature and the wind components, which are all interpolated onto the following pressure levels: 975 hPa, 925 hPa, 900 hPa., 875 hPa, 850 hPa, 800 hPa, 700 hPa, 600 hPa, 500 hPa, 400 hPa, 350 hPa, 300 hPa, 200 hPa and 100 hPa.

5. Squall line circulation reconstructions

In this section the flow fields are reconstructed on the three scale windows. For better illustration of the characteristics of the circulation, streamlines rather than wind vectors are plotted. Shown in Fig. 5a–c are the original fields at 9:30, 10:30, 11:30 UTC. We can find that, when the

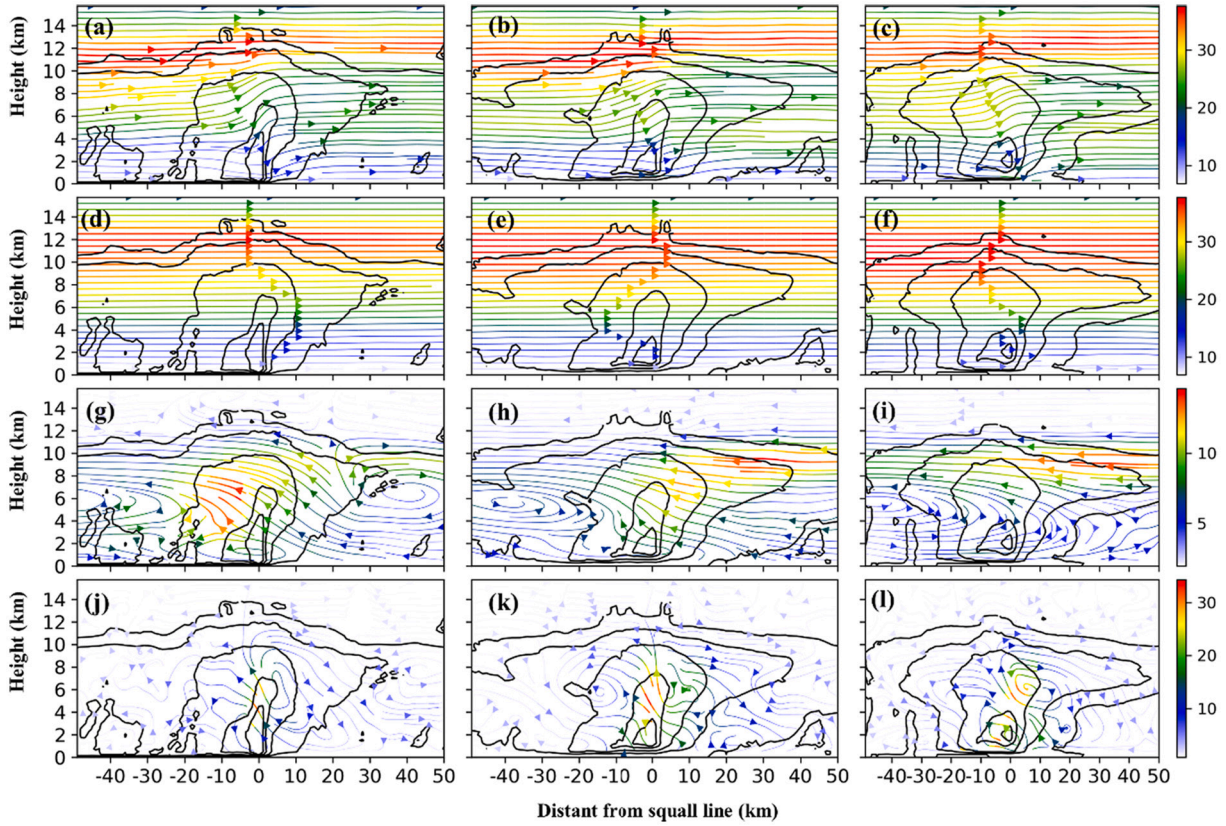

Fig. 5. The streamlines on the cross-section near the squall line. (a-c) Original fields, the wind speed ($V = \sqrt{u^2 + w^2}$) is displayed in color (m/s). (d-f) Reconstruction on the ambient flow scale window (window 0). (g-i) Reconstruction on the squall line scale window (window 1). (j-l) Reconstruction on the turbulent-scale window (window 2). The wind speed is displayed in colors (m/s). Also superimposed on the distributions is the simulated radar reflectivity (black contour lines in 10dBZ) from 09:30 through 11:30 UTC.

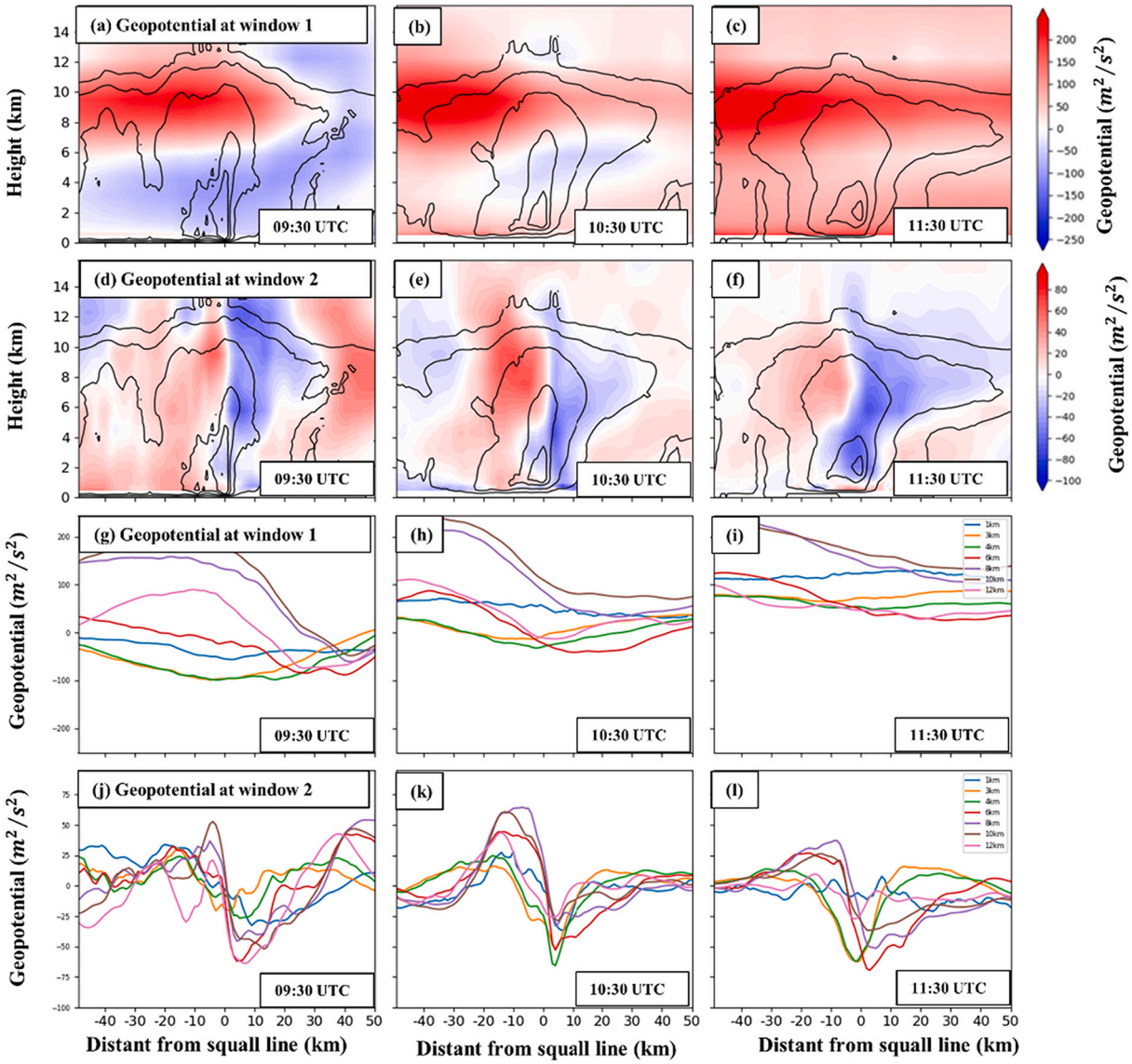

Fig. 6. The geopotential (unit: m^2/s^2) reconstructed on (a-c, g-i) window 1, and (d-f, j-i) window 2 (shaded) of the ensemble averaged cross section. The abscissa is the distance from the squall line (units: km).

squall line forms, the westerly turns updraft in the rear side near the convection center (Fig. 5a–c).

On the large scale window, the background flow remains in the form of a westerly through the depth and reaches its maximum in ~10-12 km (Fig. 5d–f). But on the squall line window, the stream line as a classical updraft and downdraft flow (Fig. 5g–i). Recall that in idealized squall line models, the inflow occurs at all levels ahead of squall line, and the outflow as a downdraft in lower level behind (Moncrieff and Miller, 1976; Gamache and Houze, 1982; Ogura and Liou, 1980). Our window 1 (squall line window) reconstructed field appears as a classical updraft-and-downdraft circulation. In this circulation, a surface-to-top updraft starts ahead of the squall line from 0 to 4 km above surface, taking off and finally flowing out from the cloud top (Fig. 5g–i). The downdraft flow behind the convective line descends from 4 km to surface (Fig. 5g–i). The window-1 reconstruction hence reveals the squall line cloud circulation. We may also find, as time goes by, the high speed center moves upward and backward into the rear portion of the leading edge (streamlines colored in red, Fig. 5g–i), similar to LeMone et al. (1984)'s description about the air parcel's accelerating path in the squall line updraft flow.

Fig. 5j–l show the window-2 reconstructions (with time scales <1.3 h). During 0930–1030 UTC (Fig. 5j–i), there is also an updraft, which is similar to that on window 1 (Fig. 5g), but limited near the convection line (the origin of the horizontal axis in Fig. 5). The upward turbulence soon sinks to the surface in both the front and rear of the squall line (Fig. 5j). At 1030UTC, the updraft becomes more vertically aligned in the leading edge (Fig. 5k). At 1130 UTC, the downdraft is enhanced and then sinks at the rear side of the leading edge (Fig. 5l).

The updraft and downdraft might be influenced by the precipitation loading and evaporative cooling caused by the severe thermodynamic effect within convective clouds, and the in-cloud turbulence can be influenced by the ambient shear wind and the cold pool (Young et al., 1995; Smull and Houze, 1985). At first, turbulence near the convective core drafts are likely to be slowly diluted from the entrainment process, which retains greater magnitudes of buoyancy and vertical motion (Morrison, 2017; Henneberg et al., 2020). As the cold pool forms, the precipitation may entrain via turbulent transport into the rear side of the leading edge (Weisman, 1992; Fan et al., 2017; Bryan and Morrison, 2012), with turbulence motion appearing more vertically and hence enhanced in sinking. These are reflected in the reconstructions as shown above.

More features can be seen from the geopotential and temperature

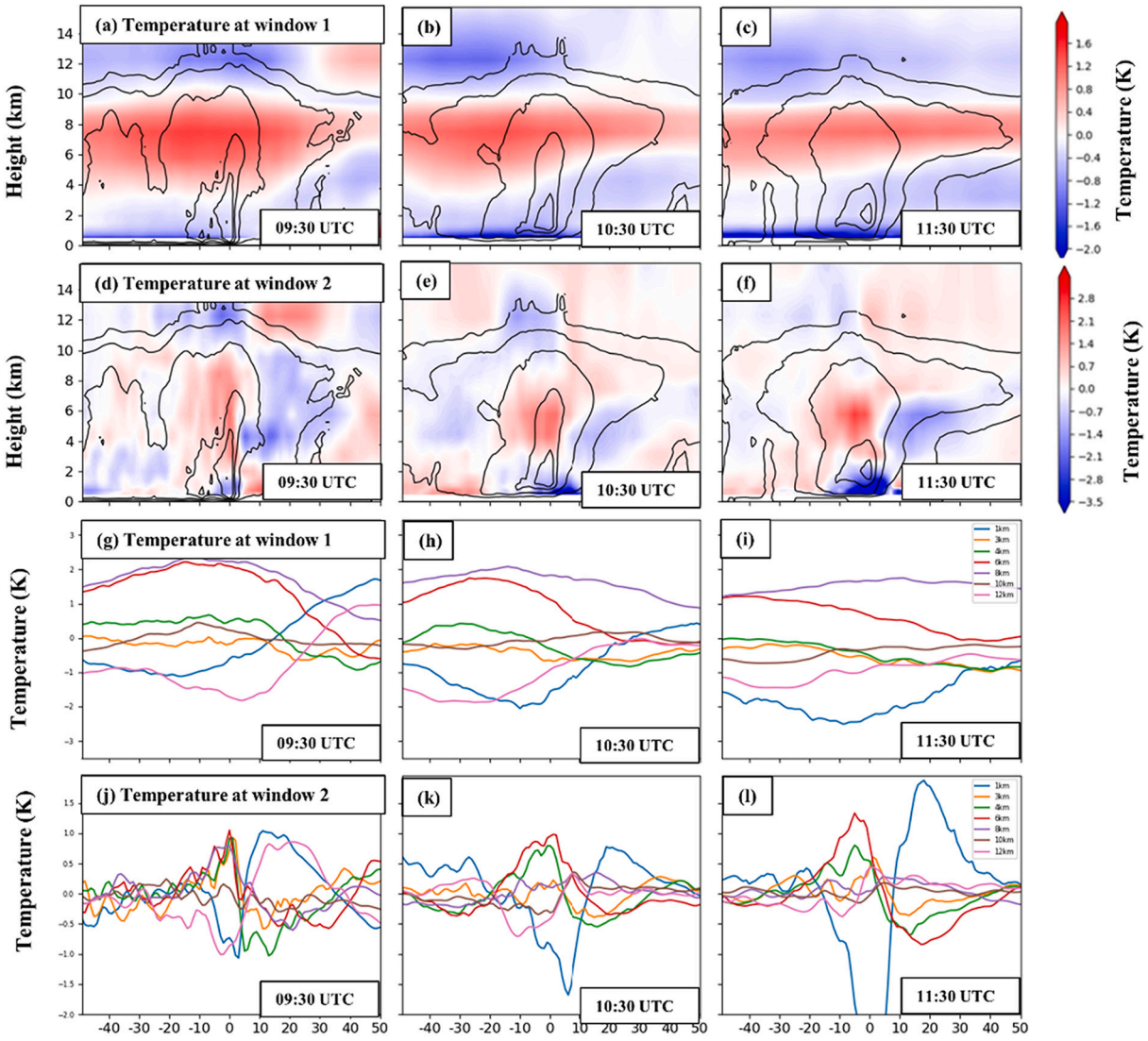

Fig. 7. Same as Fig. 6 but for temperature (units: K).

reconstructions. In Figs. 6 and 7 we plot the squall line-scale and turbulence-scale geopotential and temperature distributions. Clearly, at the surface a high pressure and a low temperature centers occur behind the leading edge on window 1 (bottom row in Figs. 6 and 7). This may be caused by the evaporation of the cold pool (Zipser, 1977; LeMone et al., 1984). The warm center on window 1 is consistent with previous studies, e.g., Gallus and Johnson (1991), who find the heating peak in high levels. And the high center of squall line-scale geopotential is also consistent with previous studies (Seigel and van den Heever, 2013).

The temperature and geopotential fields on window 2 also reveal some more features. In Figs. 6 and 7, dipoles with positive and negative centers occur (in ~6 km, 500 hPa) at both sides of the leading edge in the window-2 geopotential (Figs. 6 and 7, a–c) and temperature reconstruction fields (Figs. 6 and 7, d–f). At 11:30 UTC, the geopotential dipole becomes tilted as time goes by. This is because the negative center moves downwards to the surface, while the positive one moves upwards (Fig. 6c). At the same time, on the temperature distribution, the surface dipole is opposite to the middle-level one (Fig. 6g–i).

6. Energetics of the squall line process

As shown above, the window-1 and window-2 circulations reconstruct well the inner structures of the squall line or the storm circulation and turbulent process. In this section, we compute the kinetic energy (KE) for each scale window (Section 6.1), and study the interactions between the windows by analyzing canonical transfers (Section 6.2).

6.1. Multiscale kinetic energy

Fig. 8 shows the vertical distribution of the background KE: The right hand side is the zonal average KE, while the left hand side shows the deviation of the KE from the average. From the figure the maximum KE takes place at about 12 km corresponding to the existence of an upper jet at 200 hPa as previously reported (Xu et al., 2019). The squall line-scale KE is limited mainly at a height around 10 km (Fig. 9j–l), and the turbulence-scale KE (window 2) is centered near the convective core, with the center gradually downward from 300 hPa at 09:30 UTC to 850 hPa at 11:30 UTC (Fig. 9g–i, red & yellow line). As time moves on, both the upper center (~300 hPa, red line) and bottom center (~975 hPa, blue line) of the squall line-scale KE decrease near the leading edge (Fig. 9g–i).

6.2. Canonical transfer of KE

The canonical transfer gives a quantitative characterization of the interaction between scale windows. Particularly, as proved in Liang and

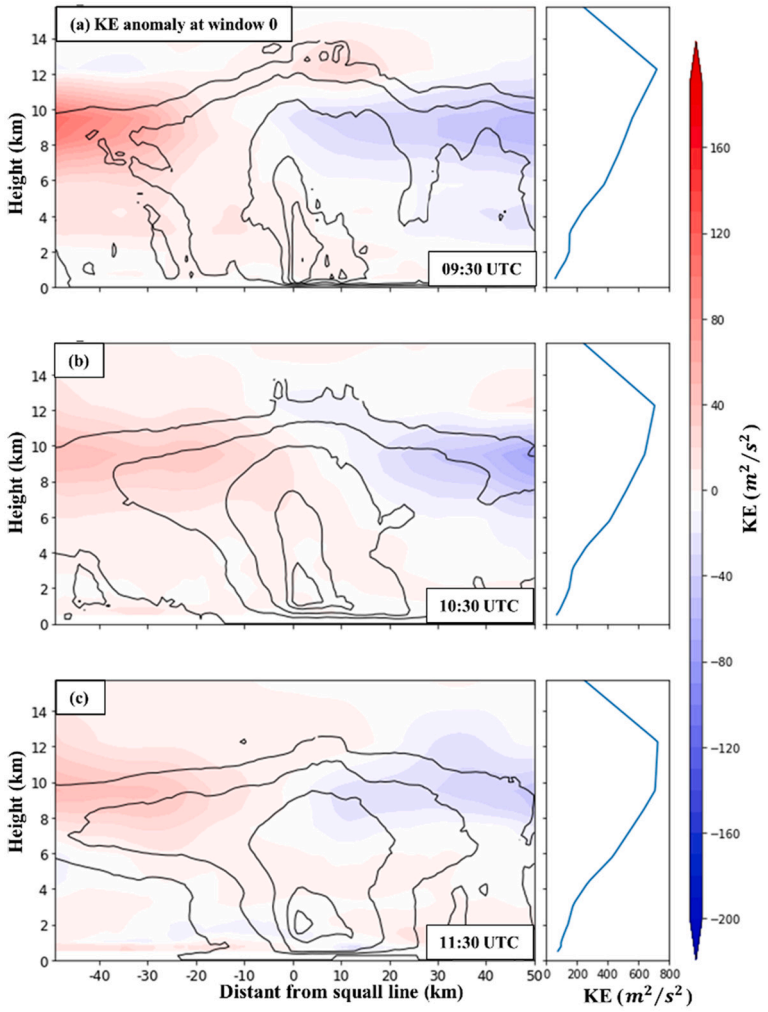

Fig. 8. Height-distance diagram of the KE anomaly on window-0 (m^2s^{-2}, left) and the horizontal-averaged (right) at (a) 09:30, (b) 10:30, and (c) 11:30 UTC.

Robinson (2007), canonical available potential energy (APE) transfer and canonical KE transfer correspond precisely to the two most important concepts in geophysical fluid dynamics, namely, baroclinic instability and barotropic instability. Here it is found that the canonical transfer of KE is as least one order greater in magnitude than that of APE (not shown), partly due to the devastatingly strong wind induced by this extreme squall line process; so the latter is negligible and will not be considered. In this subsection, we henceforth investigate the distribution of the KE canonical transfer, among others, in the hope of giving a clear energy path during the energetic cycle of the squall line process.

In a three-window framework, there are three canonical KE transfers, i.e., $\Gamma_K^{0\to1}$, $\Gamma_K^{1\to2}$, $\Gamma_K^{0\to2}$, which characterize the interaction between windows 0 and 1, that between windows 1 and 2, and that between windows 0 and 2. By computation $\Gamma_K^{0\to1}$ is negligible, and is hence not shown here. Shown in Fig. 10a–c are the distributions of $\Gamma_K^{0\to2}$ at 9:30, 10:30, 11:30 UTC, while in Fig. 10d–f are the corresponding $\Gamma_K^{1\to2}$. An observation is that they both show alternating signs with longitude. This is particularly conspicuous across the squall line. If viewed from top, they are shown on horizontal levels as dipoles through the air column, centered at the leading edge (marked as 0 km in abscissa). These dipoles are most strengthened in the mid-level (near ~500 hPa). For clarity, the 500-hPa distributions of Fig. 10a–c are plotted in Fig. 10g–i, and those of Fig. 10d–f in Fig. 10j–l. Clearly, both $\Gamma_K^{0\to2}$ and $\Gamma_K^{1\to2}$ reach their maxima at 09:30 UTC, heralding the arrival of the squall line. This makes sense, as they represent the internal dynamics which account for the emergence of these weather processes.

Another remarkable observation is that, though seemingly similar in structure, the dipoles of $\Gamma_K^{1\to2}$ and $\Gamma_K^{0\to2}$ appear mostly opposite in sign. Specifically, $\Gamma_K^{0\to2}$ (resp. $\Gamma_K^{1\to2}$) is positive (resp. negative) in the front-side of the leading edge, and negative (resp. positive) in the rear-side (e.g., Fig. 10g vs. Fig. 10j). This phenomenon can also be found from their respective horizontal distributions. Fig. 11 displays the maps of the 500-hPa maps of $\Gamma_K^{0\to2}$ and $\Gamma_K^{1\to2}$ for both Domain 1 and Domain 2. To better see this, we average the canonical transfers $\Gamma_K^{0\to2}$, $\Gamma_K^{1\to2}$, and $\Gamma_K^{0\to1}$ over time and over space in the frontal side and real side, respectively, and show the averaged values in Table 4. Since significant canonical transfers of KE are generally constrained within a width of 10 km centered on where the deepest convection occurs (Fig. 10), the spatial average is performed over −5-0 km and 0–5 km for the rear side and the front side, respectively. The result reconfirms that $\Gamma_K^{0\to1}$ is negligible, and, $\Gamma_K^{0\to2}$ and $\Gamma_K^{1\to2}$ appear opposite in sign, though the latter is one order smaller. In other words, here as the shock-like squall line propagates, KE first cascades from the ambient flow window to the turbulence window in the leading edge, which is instantaneously transferred inversely to the meso-beta-scale window (squall line window) to form the squall line; afterwards at the trailing edge the KE is transferred from the squall line window back to the turbulence window, where the turbulence-scale KE then feedbacks over the scales to the large-scale ambient flow.

The remarkable canonical transfer dipole and energy path within the squall line are consistent with those documented in the literature. Previously it has been reported that there exists a convergence-divergence

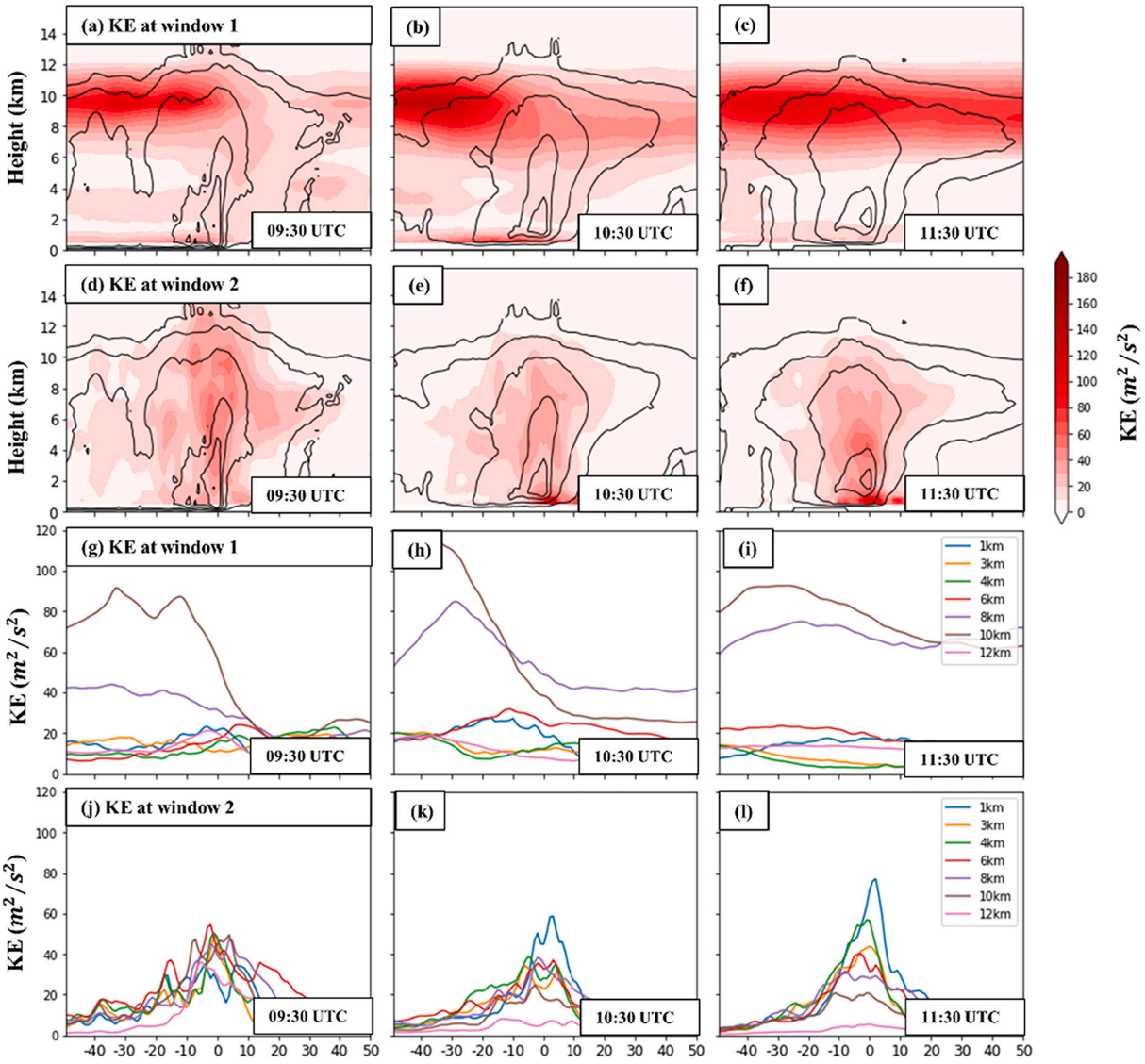

Fig. 9. Same as Fig. 6, but for KE (m^2s^{-2}).

center (Ogura and Liou, 1980): a convergence field near the gust front for the shear instability with a downscaling process, and a divergence field at the middle-to-higher levels, where the outflow in the squall line's rear-side anvil region transfers energy from the convective cells into the ambient flow (Gamache and Houze, 1982; Srivastava et al., 1986), indicating an upscaling process from the convective circulation to the ambient flow (Lafore and Moncrieff, 1989).

However, previous studies have only focused on the interactions between the ambient flow and the squall line circulation, rarely taking into account the turbulence-scale processes. In our study, the energetic pathway shows that KE is first transferred from the ambient flow window to the turbulence scale window, and then from the turbulence to the meso-beta scale window to form the squall line. That means the turbulence scale processes play an essential role in the squall line dynamics. This energetic scenario and its implication are yet to be investigated. But in recent years, several studies do confirm that selecting a higher-resolution horizontal grid spacing (which provides more turbulent scale information) can produce better simulation results for the squall line circulation (like updraft/downdraft) (Varble et al., 2020; Bryan and Morrison, 2012; Lai and Waite, 2020). This from an aspect validates our result.

The remarkable energetic scenario are also consistent with the shockwave hypothesis of squall line (Tepper, 1950). The air in the front/rear-side of the shock-wave can be compressed/inflated: the compression motions induce the downscale cascading of KE from large scales to small scales, while the expansion motions induce the upscale transferring of KE from small scales to large scales, and the two contributions are nearly equal to each other (Wang et al., 2018). The expansion/compression regions can be identified just downstream/upstream of the shocklets in the compressible isotropic turbulence, which in our case corresponds to the rear/front side of the squall line.

7. Conclusions

In this study, we simulated a devastating squall line event in southeastern China on March 4, 2018, which has incurred disastrous winds in more than four Chinese provinces. This relatively successful simulation is fully dynamical driven (no data assimilation performed), and hence allows us to gain some insight into the intrinsic processes within the squall line.

The major methodology for the dynamical study is the theory of canonical transfer based on a recently developed functional analysis apparatus, multiscale window transform. Canonical transfers result naturally from advection equations in fluid flows. A canonical transfer

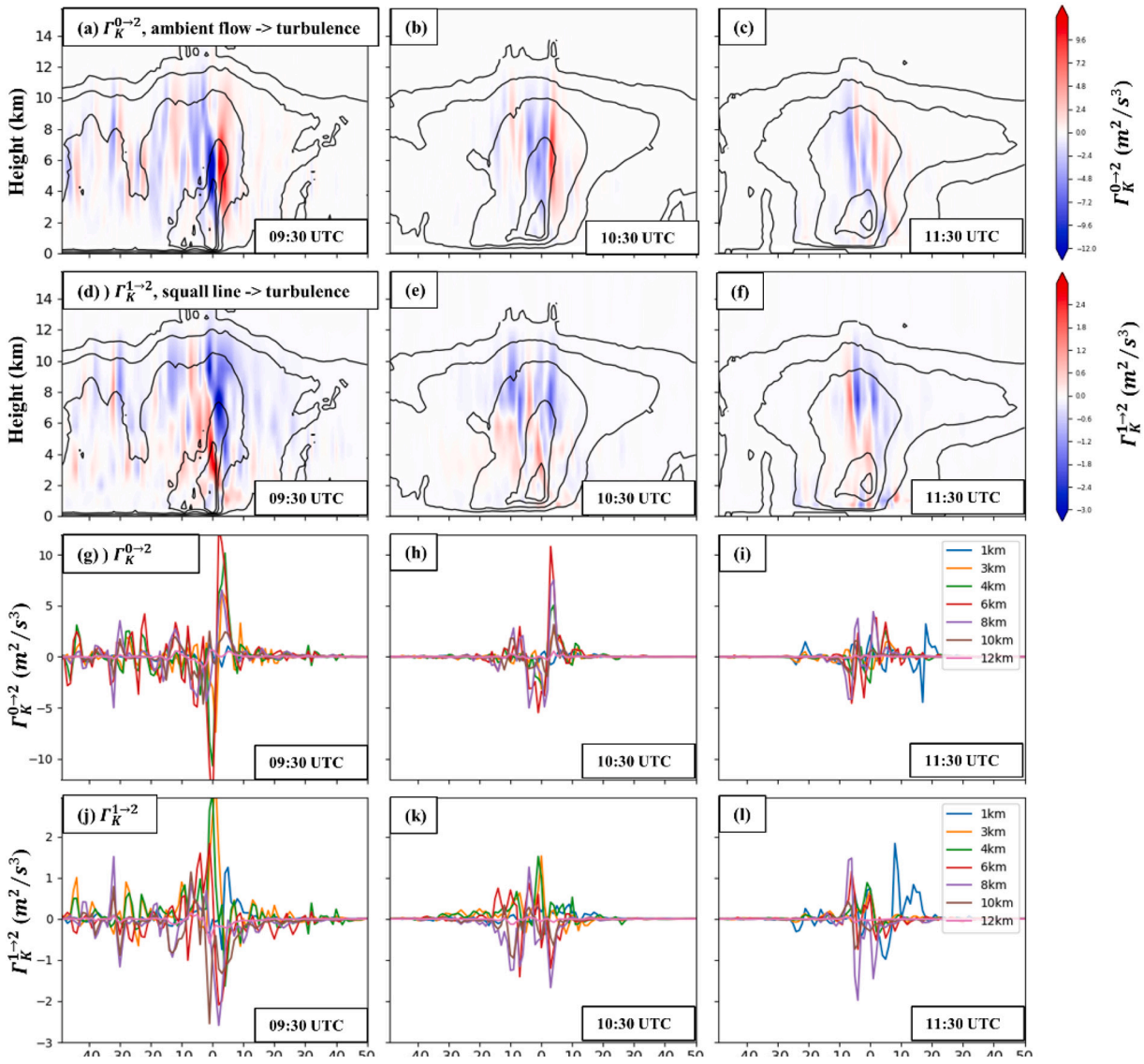

Fig. 10. As in Fig. 6, but for the canonical transfers $\Gamma_K^{0\to2}$ and $\Gamma_K^{1\to2}$(units: m^2/s^3). The other canonical transfer $\Gamma_K^{0\to1}$ is not shown as it is negligible by comparison.

bears a Lie bracket form, reminiscent of the Poisson bracket in Hamiltonian dynamics (Liang, 2016). It proves to be the faithful mechanism cascading or inversely transferring energy between two scale windows, without generating or destroying energy as a whole, in contrast to the existing empirical/engineering formalisms in the literature. In this study, three scale windows are decomposed, according to the wavelet power spectral analysis, namely, background or ambient flow window, squall line-scale window, and turbulence window. For notational convenience, these scale windows are denoted windows 0, 1, and 2, respectively. Correspondingly, a canonical transfer of kinetic energy (KE) from window i to window j is denoted $\Gamma_K^{i\to j}$, for i, j = 0, 1, 2.

It is found that, among the three canonical transfers of KE, only $\Gamma_K^{1\to2}$ and $\Gamma_K^{0\to2}$ are significant. Both are confined within the mesoscale convective systems (MCS), with sign alternating in space. They, albeit similar in structure, appear mostly opposite in sign. That is to say, a positive $\Gamma_K^{0\to2}$ corresponds remarkably well to a $\Gamma_K^{1\to2}$ in space. This is shown in both horizontal maps and vertical sections. Specifically, $\Gamma_K^{0\to2}$ (resp. $\Gamma_K^{1\to2}$) is positive (resp. negative) in the front-side, and negative (resp. positive) in the rear-side of the squall line. That is to say, at the leading edge, KE is transferred from the ambient flow over the spectrum all the way to the turbulence scale processes, and then goes to window 1 to form the squall line. At the trailing edge, this process is reversed; the KE is cascaded from the squall line to turbulence, and the turbulence-scale KE then feedbacks over the spectrum to the large-scale ambient flow. The whole process is schematized in Fig. 12.

The above remarkable finding agrees with the shock hypothesis of squall line, where at the leading edge the energy transfer is downscale while at the trailing edge it is upscale. Ideally, a shock is getting steeper and steeper at the front, whereas the rear side becomes milder and miler to form a long tail. This tells, from the energetic aspect, that the energy is transferred from large scale to small scale at the front, while at the rear side, energy is transferred from the small scale to large scale. Our opposite energy pathways across the front is in very good agreement with this conceptual scenario. What is different is that there also exists a secondary upscale transfer in the leading edge, and a downscale at the trailing edge. During the process, the turbulence-scale window functions like a hub, bridging the ambient flow and the squall line. To our knowledge, such an energetic scenario, i.e., the nexus of two adjacent scales in a spectrum via a “remote mediator” is not seen before in the literature.

The scenario revealed in Fig. 12 testifies to the importance of turbulent flows in the maintenance of squall lines. Indeed, previous studies, e.g., Varble et al. (2020) and Bryan and Morrison (2012), find that higher-resolution is needed in a model to regenerate the squall line

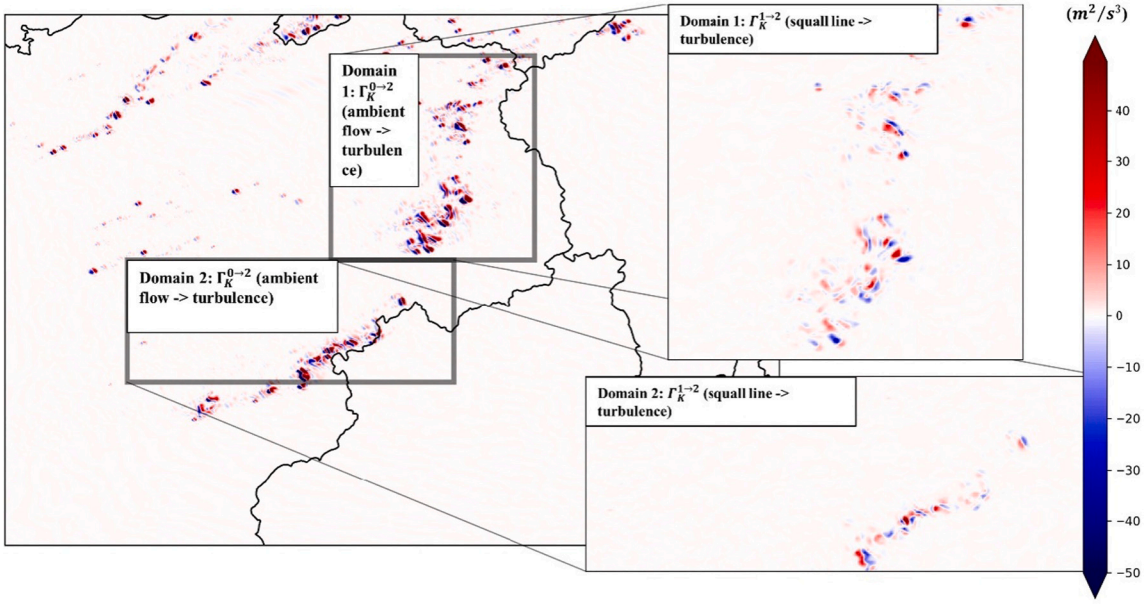

Fig. 11. A comparison between the 500-hPa $\Gamma_K^{0\to2}$ (left, in the two boxes) and $\Gamma_K^{1\to2}$ (right, in enlarged domains) at 10:30UTC. Units: m^2s^{-3}.

Table 4
Canonical transfers of KE averaged from 09:30 to 11:30 UTC (units: m^2/s^3), where the front side region and rear side region are separated at the origin of the abscissa in the figures (5 km wide each).

	$\Gamma_K^{0\to2}$	$\Gamma_K^{1\to2}$	$\Gamma_K^{0\to1}$
Front side	0.68	−0.16	0.02
Rear side	−0.75	0.14	8×10^{-5}

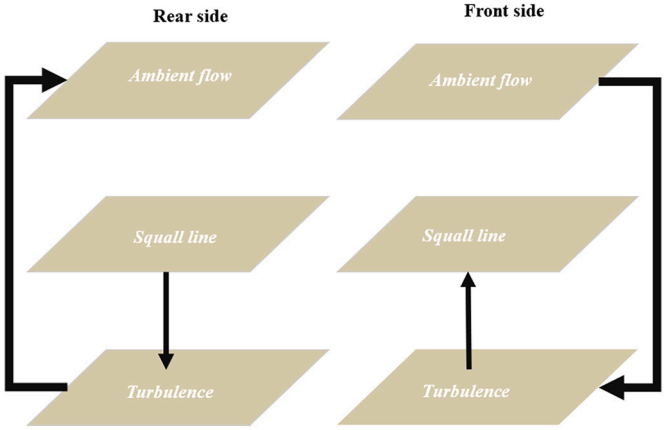

Fig. 12. A schematic of the energy pathway within the squall line.

circulation. Our study has rationalized this from a dynamical point of view, and, moreover, provided a clue to a better simulation. Of course, it is still too early to make a generalization, as currently only a particular case has been examined. We are working on more cases and looking forward to coming up with more generic conclusions.

Declaration of Competing Interest

None.

Acknowledgements

We are grateful to NCEP/FNL and China Meteorological Administration for making the data available. Thanks are due to National Center for Atmospheric Research (NCAR) for providing the WRF software. The support from the High Performance Computing Center at Nanjing University of Information Science and Technology is acknowledged. ZG thanks Yineng Rong Jiwang *Ma*, and Zhuang Zhang for their valuable inputs, and particularly appreciate the generous help from Yuhui Zhao. This study was partially supported by National Science Foundation of China under Grant #41975064, and the Fudan University Starts-up Funds to XSL.

References

Atkins, N.T., Bouchard, C.S., Przybylinski, R.W., Trapp, R.J., Schmocker, G., 2005. Damaging Surface Wind Mechanisms within the 10 June 2003 Saint Louis Bow Echo during BAMEX. Mon. Weather Rev. 133, 2275–2296. https://doi.org/10.1175/MWR2973.1.

Benjamin, T.B., 1968. Gravity currents and related phenomena. J. Fluid Mech. 31, 209–248. https://doi.org/10.1017/S0022112068000133.

Bou-Zeid, E., Meneveau, C., Parlange, M.B. (Eds.), 2005. A scale-dependent Lagrangian dynamic model for large eddy simulation of complex turbulent flows. Phys. Fluids. https://doi.org/10.1063/1.1839152.

Bryan, G.H., Morrison, H., 2012. Sensitivity of a simulated squall line to horizontal resolution and parameterization of microphysics. Mon. Weather Rev. 140, 202–225. https://doi.org/10.1175/MWR-D-11-00046.1.

Bryan, G.H., Wyngaard, J.C., Fritsch, J.M., 2003. Resolution requirements for the simulation of deep moist convection. Mon. Weather Rev. 131, 2394–2416. https://doi.org/10.1175/1520-0493(2003)131<2394:RRFTSO>2.0.CO;2.

Charba, J., 1974. Application of gravity current model to analysis of squall-line gust front. Mon. Weather Rev. 102, 140. https://doi.org/10.1175/1520-0493(1974)102<0140:AOGCMT>2.0.CO;2.

Chow, F.K., Street, R.L., Xue, M., Ferziger, J.H., 2005. Explicit filtering and reconstruction turbulence modeling for large-eddy simulation of neutral boundary layer flow. J. Atmos. Sci. 62, 2058–2077. https://doi.org/10.1175/JAS3456.1.

Deardorff, J.W., 1980. Stratocumulus-capped mixed layers derived from a three-dimensional model. Bound.-Layer Meteorol. 18, 495–527. https://doi.org/10.1007/BF00119502.

Ducrocq, V., Bougeault, P., 1995. Simulation of an observed squall line with a meso-beta-scale hydrostatic model. Weather Forecast. 10, 380–399. https://doi.org/10.1175/1520-0434(1995)010<0380:SOAOSL>2.0.CO;2.

Dudhia, J., 1989. Numerical study of convection observed during the winter monsoon experiment using a mesoscale two-dimensional model. J. Atmos. Sci. 46, 3077–3107. https://doi.org/10.1175/1520-0469(1989)046<3077:NSOCOD>2.0.CO;2.

Fan, J., Han, B., Varble, A., Morrison, H., North, K., Kollias, P., Chen, B., Dong, X., Giangrande, S.E., Khain, A., Lin, Y., Mansell, E., Milbrandt, J.A., Stenz, R., Thompson, G., Wang, Y., 2017. Cloud-resolving model intercomparison of an MC3E

squall line case: Part I—convective updrafts. J. Geophys. Res. Atmos. 122, 9351–9378. https://doi.org/10.1002/2017JD026622.
Frame, J., Markowski, P., 2006. The interaction of simulated squall lines with idealized mountain ridges. Mon. Weather Rev. 134, 1919–1941. https://doi.org/10.1175/MWR3157.1.
Fujita, T.T., 1978. Manual of Downburst Identification for Project NIMROD (No. NASA-CR-156953).
Gallus, W.A., Johnson, R.H., 1991. Heat and moisture budgets of an intense midlatitude squall line. J. Atmos. Sci. 48, 122–146. https://doi.org/10.1175/1520-0469(1991)048<0122:HAMBOA>2.0.CO;2.
Gamache, J.F., Houze, R.A., 1982. Mesoscale air motions associated with a tropical squall line. Mon. Weather Rev. 110, 118–135. https://doi.org/10.1175/1520-0493(1982)110<0118:MAMAWA>2.0.CO;2.
Henneberg, O., Meyer, B., Haerter, J.O., 2020. Particle-based tracking of cold pool gust fronts. J. Adv. Model. Earth Syst. 12 https://doi.org/10.1029/2019MS001910 e2019MS001910.
Holopainen, E.O., 1978. On the dynamic forcing of the long-term mean flow by the large-scale reynolds' stresses in the atmosphere. J. Atmos. Sci. 35, 1596–1604. https://doi.org/10.1175/1520-0469(1978)035<1596:OTDFOT>2.0.CO;2.
Houze, R.A., Smull, B.F., Dodge, P., 1990. Mesoscale organization of springtime rainstorms in oklahoma. Mon. Weather Rev. 118, 613–654. https://doi.org/10.1175/1520-0493(1990)118<0613:MOOSRI>2.0.CO;2.
Janjić, Z.I., 1994. The step-mountain eta coordinate model: further developments of the convection, viscous sublayer, and turbulence closure schemes. Mon. Weather Rev. 122, 927–945. https://doi.org/10.1175/1520-0493(1994)122<0927:TSMECM>2.0.CO;2.
Kain, J.S., 2004. The Kain–Fritsch convective parameterization: an update. J. Appl. Meteorol. Climatol. 43, 170–181. https://doi.org/10.1175/1520-0450(2004)043<0170:TKCPAU>2.0.CO;2.
Kirkil, G., Mirocha, J., Bou-Zeid, E., Chow, F.K., Kosović, B., 2012. Implementation and evaluation of dynamic subfilter-scale stress models for large-eddy simulation using WRF. Mon. Weather Rev. 140, 266–284. https://doi.org/10.1175/MWR-D-11-00037.1.
Kosović, B., 1997. Subgrid-scale modelling for the large-eddy simulation of high-Reynolds-number boundary layers. J. Fluid Mech. 336, 151–182. https://doi.org/10.1017/S0022112096004697.
Kraichnan, R.H., 1976. Eddy viscosity in two and three dimensions. J. Atmos. Sci. 33, 1521–1536. https://doi.org/10.1175/1520-0469(1976)033<1521:EVITAT>2.0.CO;2.
Lafore, J.-P., Moncrieff, M.W., 1989. A numerical investigation of the organization and interaction of the convective and stratiform regions of tropical squall lines. J. Atmos. Sci. 46, 521–544. https://doi.org/10.1175/1520-0469(1989)046<0521:ANIOTO>2.0.CO;2.
Lai, K.T., Waite, M.L., 2020. Resolution dependence and subfilter-scale motions in idealized squall-line simulations. Mon. Weather Rev. 148, 3059–3078. https://doi.org/10.1175/MWR-D-19-0330.1.
Lane, T.P., Sharman, R.D., Trier, S.B., Fovell, R.G., Williams, J.K., 2012. Recent advances in the understanding of near-cloud turbulence. Bull. Am. Meteorol. Soc. 93, 499–515. https://doi.org/10.1175/BAMS-D-11-00062.1.
Lebo, Z.J., Morrison, H., 2015. Effects of horizontal and vertical grid spacing on mixing in simulated squall lines and implications for convective strength and structure. Mon. Weather Rev. 143, 4355–4375. https://doi.org/10.1175/MWR-D-15-0154.1.
Leith, C.E., 1990. Stochastic backscatter in a subgrid-scale model: plane shear mixing layer. Phys. Fluids Fluid Dyn. 2, 297–299. https://doi.org/10.1063/1.857779.
LeMone, M.A., Barnes, G.M., Zipser, E.J., 1984. Momentum flux by lines of cumulonimbus over the tropical oceans. J. Atmos. Sci. 41, 1914–1932. https://doi.org/10.1175/1520-0469(1984)041<1914:MFBLOC>2.0.CO;2.
Li, B., Wu, L., 2020. Numerical study of effects of mountains and lakes on a squall line in northern Jiangsu Province. Meteorol. Atmospheric Phys. 132, 781–791. https://doi.org/10.1007/s00703-019-00721-5.
Liang, X.S., 2016. Canonical transfer and multiscale energetics for primitive and quasigeostrophic atmospheres. J. Atmos. Sci. 73, 4439–4468. https://doi.org/10.1175/JAS-D-16-0131.1.
Liang, X.S., Anderson, D.G.M., 2007. Multiscale window transform. Multiscale Model. Simul. 6, 437–467. https://doi.org/10.1137/06066895X.
Liang, X.S., Robinson, A.R., 2005. Localized multiscale energy and vorticity analysis: I. Fundamentals. Dyn. Atmos. Oceans 38, 195–230. https://doi.org/10.1016/j.dynatmoce.2004.12.004.
Liang, X.S., Robinson, A.R., 2007. Localized multi-scale energy and vorticity analysis: II. Finite-amplitude instability theory and validation. Dyn. Atmos. Oceans 44, 51–76. https://doi.org/10.1016/j.dynatmoce.2007.04.001.
Lilly, D.K., 1990. Numerical prediction of thunderstorms—has its time come? Q. J. R. Meteorol. Soc. 116, 779–798. https://doi.org/10.1002/qj.49711649402.
Lindzen, R.S., Tung, K.-K., 1976. Banded convective activity and ducted gravity waves. Mon. Weather Rev. 104, 1602–1617. https://doi.org/10.1175/1520-0493(1976)104<1602:BCAADG>2.0.CO;2.
Lynn, B.H., Khain, A.P., Dudhia, J., Rosenfeld, D., Pokrovsky, A., Seifert, A., 2005a. Spectral (Bin) microphysics coupled with a mesoscale model (MM5). Part II: simulation of a CaPE rain event with a squall line. Mon. Weather Rev. 133, 59–71. https://doi.org/10.1175/MWR-2841.1.
Lynn, B.H., Khain, A.P., Dudhia, J., Rosenfeld, D., Pokrovsky, A., Seifert, A., 2005b. Spectral (Bin) microphysics coupled with a mesoscale model (MM5). Part I: model description and first results. Mon. Weather Rev. 133, 44–58. https://doi.org/10.1175/MWR-2840.1.
Majda, A.J., Xing, Y., 2010. New multi-scale models on mesoscales and squall lines. Commun. Math. Sci. 8, 113–134.
Meng, Z., Yan, D., Zhang, Y., 2013. General features of squall lines in East China. Mon. Weather Rev. 141, 1629–1647. https://doi.org/10.1175/MWR-D-12-00208.1.
Mlawer, E.J., Taubman, S.J., Brown, P.D., Iacono, M.J., Clough, S.A., 1997. Radiative transfer for inhomogeneous atmospheres: RRTM, a validated correlated-k model for the longwave. J. Geophys. Res. Atmos. 102, 16663–16682. https://doi.org/10.1029/97JD00237.
Moeng, C.-H., LeMone, M.A., Khairoutdinov, M.F., Krueger, S.K., Bogenschutz, P.A., Randall, D.A., 2009. The tropical marine boundary layer under a deep convection system: a large-eddy simulation study. J. Adv. Model. Earth Syst. 1 https://doi.org/10.3894/JAMES.2009.1.16.
Moeng, C.-H., Sullivan, P.P., Khairoutdinov, M.F., Randall, D.A., 2010. A mixed scheme for subgrid-scale fluxes in cloud-resolving models. J. Atmos. Sci. 67, 3692–3705. https://doi.org/10.1175/2010JAS3565.1.
Moncrieff, M.W., Miller, M.J., 1976. The dynamics and simulation of tropical cumulonimbus and squall lines. Q. J. R. Meteorol. Soc. 102, 373–394. https://doi.org/10.1002/qj.49710243208.
Morrison, H., 2017. An analytic description of the structure and evolution of growing deep cumulus updrafts. J. Atmos. Sci. 74, 809–834. https://doi.org/10.1175/JAS-D-16-0234.1.
Morrison, H., Thompson, G., Tatarskii, V., 2009. Impact of cloud microphysics on the development of trailing stratiform precipitation in a simulated squall line: comparison of one- and two-moment schemes. Mon. Weather Rev. 137, 991–1007. https://doi.org/10.1175/2008MWR2556.1.
Niu, G.-Y., Yang, Z.-L., Mitchell, K.E., Chen, F., Ek, M.B., Barlage, M., Kumar, A., Manning, K., Niyogi, D., Rosero, E., Tewari, M., Xia, Y., 2011. The community Noah land surface model with multiparameterization options (Noah-MP): 1. Model description and evaluation with local-scale measurements. J. Geophys. Res. Atmos. 116. https://doi.org/10.1029/2010JD015139.
Nolen, R.H., 1959. A radar pattern associated with tornadoes. Bull. Am. Meteorol. Soc. 40, 277–279. https://doi.org/10.1175/1520-0477-40.6.277.
Ogura, Y., Liou, M.-T., 1980. The structure of a midlatitude squall line: a case study. J. Atmos. Sci. 37, 553–567. https://doi.org/10.1175/1520-0469(1980)037<0553:TSOAMS>2.0.CO;2.
Orlanski, I., 1975. A rational subdivision of scales for atmospheric processes. Bull. Am. Meteorol. Soc. 56, 527–530.
Pantley, K.C., Lester, P.F., 1990. Observations of severe turbulence near thunderstorm tops. J. Appl. Meteorol. Climatol. 29, 1171–1179. https://doi.org/10.1175/1520-0450(1990)029<1171:OOSTNT>2.0.CO;2.
Parker, M.D., Johnson, R.H., 2000. Organizational modes of midlatitude mesoscale convective systems. Mon. Weather Rev. 128, 3413–3436. https://doi.org/10.1175/1520-0493(2001)129<3413:OMOMMC>2.0.CO;2.
Piomelli, U., Cabot, W.H., Moin, P., Lee, S., 1991. Subgrid-scale backscatter in turbulent and transitional flows. Phys. Fluids Fluid Dyn. 3, 1766–1771. https://doi.org/10.1063/1.857956.
Plumb, R.A., 1983. A new look at the energy cycle. J. Atmos. Sci. 40, 1669–1688. https://doi.org/10.1175/1520-0469(1983)040<1669:ANLATE>2.0.CO;2.
Pope, S., 2004. Ten questions concerning the Large-Eddy simulation of turbulent flows. New J. Phys. 6 https://doi.org/10.1088/1367-2630/6/1/035.
Potvin, C.K., Flora, M.L., 2015. Sensitivity of idealized supercell simulations to horizontal grid spacing: implications for warn-on-forecast. Mon. Weather Rev. 143, 2998–3024. https://doi.org/10.1175/MWR-D-14-00416.1.
Przybylinski, R.W., 1995. The bow echo: observations, numerical simulations, and severe weather detection methods. Weather Forecast. 10, 203–218. https://doi.org/10.1175/1520-0434(1995)010<0203:TBEONS>2.0.CO;2.
Rotunno, R., Klemp, J.B., Weisman, M.L., 1988. A theory for strong, long-lived squall lines. J. Atmos. Sci. 45, 463–485. https://doi.org/10.1175/1520-0469(1988)045<0463:ATFSLL>2.0.CO;2.
Schumann, U., 1995. Stochastic Backscatter of Turbulence Energy and Scalar Variance by Random Subgrid-Scale Fluxes.
Seigel, R.B., van den Heever, S.C., 2013. Squall-line intensification via hydrometeor recirculation. J. Atmos. Sci. 70, 2012–2031. https://doi.org/10.1175/JAS-D-12-0266.1.
Sheng, J., 2019. Evolution and Mechanism of a Rare Squall Line in China of 2018, 2019, pp. A53U–3057.
Skamarock, W., Klemp, J., Dudhia, J., Gill, D., Barker, D., Wang, W., Huang, X.-Y., Duda, M., 2008. A Description of the Advanced Research WRF Version 3. UCAR/NCAR. https://doi.org/10.5065/D68S4MVH.
Smagorinsky, J., 1963. General circulation experiments with the primitive equations: I. The basic experiment. Mon. Weather Rev. 91, 99–164. https://doi.org/10.1175/1520-0493(1963)091<0099:GCEWTP>2.3.CO;2.
Smull, B.F., Houze, R.A., 1985. A midlatitude squall line with a trailing region of stratiform rain: Radar and satellite observations. Mon. Weather Rev. 113, 117–133. https://doi.org/10.1175/1520-0493(1985)113<0117:AMSLWA>2.0.CO;2.
Srivastava, R.C., Matejka, T.J., Lorello, T.J., 1986. Doppler radar study of the trailing anvil region associated with a squall line. J. Atmos. Sci. 43, 356–377. https://doi.org/10.1175/1520-0469(1986)043<0356:DRSOTT>2.0.CO;2.
Tepper, M., 1950. A proposed mechanism of squall lines: the pressure jump line. J. Atmos. Sci. 7, 21–29. https://doi.org/10.1175/1520-0469(1950)007<0021:APMOSL>2.0.CO;2.
Varble, A., Morrison, H., Zipser, E., 2020. Effects of under-resolved convective dynamics on the evolution of a squall line. Mon. Weather Rev. 148, 289–311. https://doi.org/10.1175/MWR-D-19-0187.1.
Wakimoto, R.M., Murphey, H.V., Davis, C.A., Atkins, N.T., 2006a. High winds generated by bow echoes. Part II: the relationship between the mesovortices and damaging straight-line winds. Mon. Weather Rev. 134, 2813–2829. https://doi.org/10.1175/MWR3216.1.

Wakimoto, R.M., Murphey, H.V., Nester, A., Jorgensen, D.P., Atkins, N.T., 2006b. High winds generated by bow echoes. Part I: Overview of the Omaha Bow Echo 5 July 2003 storm during BAMEX. Mon. Weather Rev. 134, 2793–2812. https://doi.org/10.1175/MWR3215.1.

Wang, J., Wan, M., Chen, Song, Chen, Shiyi, 2018. Kinetic energy transfer in compressible isotropic turbulence. J. Fluid Mech. 841, 581–613. https://doi.org/10.1017/jfm.2018.23.

Weisman, M.L., 1992. The role of convectively generated rear-inflow jets in the evolution of long-lived mesoconvective systems. J. Atmos. Sci. 49, 1826–1847. https://doi.org/10.1175/1520-0469(1992)049<1826:TROCGR>2.0.CO;2.

Weisman, M.L., Davis, C.A., 1998. Mechanisms for the generation of mesoscale vortices within quasi-linear convective systems. J. Atmos. Sci. 55, 2603–2622. https://doi.org/10.1175/1520-0469(1998)055<2603:MFTGOM>2.0.CO;2.

Weisman, M.L., Skamarock, W.C., Klemp, J.B., 1997. The resolution dependence of explicitly modeled convective systems. Mon. Weather Rev. 125, 527–548. https://doi.org/10.1175/1520-0493(1997)125<0527:TRDOEM>2.0.CO;2.

Weisman, M.L., Davis, C., Wang, W., Manning, K.W., Klemp, J.B., 2008. Experiences with 0–36-h explicit convective forecasts with the WRF-ARW model. Weather Forecast. 23, 407–437. https://doi.org/10.1175/2007WAF2007005.1.

Wyngaard, J.C., 2004. Toward numerical modeling in the "Terra Incognita". J. Atmos. Sci. 61, 1816–1826. https://doi.org/10.1175/1520-0469(2004)061<1816:TNMITT>2.0.CO;2.

Xu, Q., Moncrieff, M.W., 1994. Density current circulations in shear flows. J. Atmos. Sci. 51, 434–446. https://doi.org/10.1175/1520-0469(1994)051<0434:DCCISF>2.0.CO;2.

Xu, B., Xu, A., Chen, Y., Xiang Xiang, C., 2019. Application of severe convective weather conceptual model in the prediction of "3.4" extreme gale in Jiangxi. J. Rainstorm Disaster. 38, 114–151.

Young, G.S., Perugini, S.M., Fairall, C.W., 1995. Convective wakes in the equatorial western pacific during TOGA. Mon. Weather Rev. 123, 110–123. https://doi.org/10.1175/1520-0493(1995)123<0110:CWITEW>2.0.CO;2.

Zhang, X., Zhou, B., Ping, F., 2021. Effects of subgrid-scale horizontal turbulent mixing on a simulated convective storm at kilometer-scale resolutions. Atmos. Res. 254, 105445 https://doi.org/10.1016/j.atmosres.2020.105445.

Zhu, P., Hazelton, A., Zhang, Z., Marks, F.D., Tallapragada, V., 2021. The role of eyewall turbulent transport in the pathway to intensification of tropical cyclones. J. Geophys. Res. Atmos. 126 https://doi.org/10.1029/2021JD034983 e2021JD034983.

Zipser, E.J., 1977. Mesoscale and convective–scale downdrafts as distinct components of squall-line structure. Mon. Weather Rev. 105, 1568–1589. https://doi.org/10.1175/1520-0493(1977)105<1568:MACDAD>2.0.CO;2.